

THE VELA-X PULSAR WIND NEBULA REVISITED WITH FOUR YEARS OF *FERMI* LARGE AREA TELESCOPE OBSERVATIONS

M.-H. GRONDIN^{1,6}, R. W. ROMANI², M. LEMOINE-GOUMARD^{3,7}, L. GUILLEMOT⁴, A. K. HARDING⁵, AND T. REPOSEUR³

¹ Max-Planck-Institut für Kernphysik, P.O. Box 103980, D-69029 Heidelberg, Germany; mgrondin@irap.omp.eu

² W. W. Hansen Experimental Physics Laboratory, Kavli Institute for Particle Astrophysics and Cosmology, Department of Physics and SLAC National Accelerator Laboratory, Stanford University, Stanford, CA 94305, USA

³ Université Bordeaux 1, CNRS/IN2p3, Centre d'Études Nucléaires de Bordeaux Gradignan, F-33175 Gradignan, France

⁴ Max-Planck-Institut für Radioastronomie, Auf dem Hügel 69, D-53121 Bonn, Germany

⁵ NASA Goddard Space Flight Center, Greenbelt, MD 20771, USA

Received 2013 February 20; accepted 2013 July 19; published 2013 August 21

ABSTRACT

The Vela supernova remnant (SNR) is the closest SNR to Earth containing an active pulsar, the Vela pulsar (PSR B0833–45). This pulsar is an archetype of the middle-aged pulsar class and powers a bright pulsar wind nebula (PWN), Vela-X, spanning a region of $2^\circ \times 3^\circ$ south of the pulsar and observed in the radio, X-ray, and very high energy γ -ray domains. The detection of the Vela-X PWN by the *Fermi* Large Area Telescope (LAT) was reported in the first year of the mission. Subsequently, we have reinvestigated this complex region and performed a detailed morphological and spectral analysis of this source using 4 yr of *Fermi*-LAT observations. This study lowers the threshold for morphological analysis of the nebula from 0.8 GeV to 0.3 GeV, allowing for the inspection of distinct energy bands by the LAT for the first time. We describe the recent results obtained on this PWN and discuss the origin of the newly detected spatial features.

Key words: gamma rays: general – ISM: individual objects (Vela-X) – pulsars: general – pulsars: individual (Vela, PSR J0835–4510)

Online-only material: color figures

1. INTRODUCTION

The supernova remnant (SNR) G263.9–3.3 (aka the Vela SNR) is the closest composite SNR to Earth containing an active pulsar, the Vela pulsar (PSR B0833–45), and is therefore studied in great detail across the electromagnetic spectrum. Located at a distance of only $D = 290$ pc (Caraveo et al. 2001; Dodson et al. 2003), the Vela pulsar has a characteristic age of $\tau_c = 11$ kyr, a spin period of $P = 89$ ms, and a spin-down power of $\dot{E} = 7 \times 10^{36}$ erg s^{−1}. First discovered as a radio-loud pulsar (Large et al. 1968), its pulsations were successively detected in high-energy (HE) γ -rays (Thompson, 1975), optical (Wallace et al. 1977), and X-rays (Ögelman et al. 1993). Recent γ -ray observations by the *Fermi* Large Area Telescope (LAT) have confirmed its detection above 20 MeV and enabled a more detailed study of its γ -ray properties than possible with the previous missions SAS-II, COS-B, and CGRO-EGRET (Kanbach et al. 1994 and references therein). These observations reveal a magnetospheric emission over 80% of the pulsar period, and a strong and complex phase dependence of the γ -ray spectrum, in particular in the peaks of the light curve (Abdo et al. 2009b, 2010a).

The 8° diameter Vela SNR is also known to host several regions of non-thermal and diffuse radio emission labeled Vela-X, Vela-Y, and Vela-Z (Rishbeth, 1958). The brightest one (~ 1000 Jy), Vela-X, spans a region of $2^\circ \times 3^\circ$ (referred to as the “halo”) surrounding the Vela pulsar and shows a filamentary structure. In particular, the brightest radio filament has an extent of $45' \times 12'$ and is located south of the pulsar. The flat spectrum of Vela-X with respect to Vela-Y and Vela-Z and its high

degree of radio polarization have led to strong presumptions that Vela-X is the pulsar wind nebula (PWN) associated with the energetic and middle-aged Vela pulsar (Weiler & Panagia 1980). The rotational energy of the pulsar is dissipated through a magnetized wind of relativistic particles. A PWN forms at the termination shock resulting from the interaction between the relativistic wind and the surrounding material, e.g., the supernova ejecta (Gaensler & Slane, 2006).

Following its radio discovery, the Vela-X region has been intensively observed at every wavelength. X-ray observations by *ROSAT* have unveiled a diffuse and nebular emission (with an extent of 1.5×0.5) coincident with the bright radio filament and referred to as the “cocoon” (Markwardt & Ögelman 1995). The Vela-X region has been significantly detected up to 0.4 MeV by *OSSE* with a spectrum consistent with the $E^{-1.7}$ spectrum seen between optical and X-rays (de Jager et al. 1996). High-resolution *Chandra* observations have enabled the detection of bright and compact non-thermal X-ray emission composed of two toroidal arcs ($17''$ and $30''$ away from the pulsar) and a $4'$ long collimated “jet”-like structure (Helfand et al. 2001). Finally, very high energy (VHE) γ -ray observations by the H.E.S.S. telescopes have revealed bright emission spatially coincident with the cocoon, whose spectrum peaks at ~ 10 TeV (Aharonian et al. 2006). This detection has confirmed the non-thermal nature of the cocoon; however, the relativistic particle population responsible for the X-ray and TeV emission can hardly account for the halo structure observed in radio.

At this time, several scenarios have been proposed to reconcile multi-wavelength data. Horns et al. (2006) proposed a hadronic model, in which the VHE γ -ray emission is explained by proton–proton interactions inside the cocoon followed by neutral pion decays. In parallel, de Jager et al. (2008) suggested the existence of two electron populations in Vela-X: a young

⁶ Now at CNRS, IRAP, F-31028 Toulouse cedex 4, France/GAHEC, Université de Toulouse, UPS-OMP, IRAP, Toulouse, France.

⁷ Funded by contract ERC-StG-259391 from the European Community.

population that produces the narrow cocoon seen in X-rays and at VHE, and a relic one responsible for the extended halo observed in radio. According to this model, significant emission from the halo should be detectable in the *Fermi*-LAT energy range. An alternative scenario was recently proposed by Hinton et al. (2011), which explains the observations by diffusive escape of particles in the extended halo structure.

The first HE γ -ray detection of the Vela-X PWN by the *Fermi*-LAT was reported in the first year of the mission. The source is significantly extended (with an extension of $\sigma_{\text{Disk}} = 0^{\circ}.88 \pm 0^{\circ}.12$ assuming a uniform disk hypothesis) and its spectrum is well reproduced with a simple power law having a soft index ($\Gamma \sim 2.41 \pm 0.09_{\text{stat}} \pm 0.15_{\text{sys}}$) in the 0.2–20 GeV energy range (Abdo et al. 2010b). The detection of Vela-X in the 0.1–3 GeV energy range was also reported by the AGILE Collaboration (Pellizzoni et al. 2010).

Abramowski et al. (2012) recently reported the detection of faint TeV emission spatially coincident with the radio halo, in addition to the bright emission already reported and matching the X-ray emission. This new result challenges the simple interpretation of a young electron population being responsible for the X-ray and VHE emission.

We have reinvestigated this complex region in HE γ -rays and performed a detailed morphological and spectral analysis of this source using four years of *Fermi*-LAT observations. The energy range for morphological analysis is extended down to 0.3 GeV allowing for the first study of energy-dependent morphology by the LAT. In this paper, we report the results of this analysis and discuss the main implications of the new spectrally resolved spatial information in the context of the theoretical models described above. In particular, we discuss the possible interpretation of the energy-dependent morphology brought to light with four years of *Fermi*-LAT observations.

2. LAT DESCRIPTION AND OBSERVATIONS

The LAT is a γ -ray telescope that detects photons by conversion into electron–positron pairs and operates in the energy range from 20 MeV to greater than 300 GeV. Details of the instrument and data processing are given in Atwood et al. (2009). The on-orbit calibration is described in Abdo et al. (2009a) and Ackermann et al. (2012).

The following analysis was performed using 48 months of data collected starting 2008 August 4, and extending until 2012 August 4 within a $15^{\circ} \times 15^{\circ}$ region around the position of the Vela pulsar.

Only γ -rays in the from the Pass 7 “Source” class were selected from this sample. This class corresponds to a good compromise between the number of selected photons and the background rate. We have used the P7SOURCE_V6 instrument response functions (IRFs) to perform the following analyses. We excluded photons with zenith angles greater than 100° to reduce contamination from secondary γ -rays originating in Earth’s atmosphere (Abdo et al. 2009a).

3. TIMING ANALYSIS OF THE PULSAR PSR J0835–4510

The Vela pulsar is the brightest steady point source in the γ -ray sky, with pulsed photons observed up to 25 GeV, and is located within the Vela-X PWN. Previous analyses of its γ -ray properties using *Fermi*-LAT observations have shown that magnetospheric emission is observed over 80% of the pulsar period (Abdo et al. 2010a).

The detailed study of Vela-X requires working in the off-pulse window of the Vela pulsar light curve (i.e., 20% of the pulsar period) to avoid contamination from the pulsed emission. Because the Vela pulsar exhibits substantial timing irregularities, phase assignment generally requires a contemporary ephemeris. To perform the following analysis, γ -ray photons were phase-folded using an accurate timing solution derived from *Fermi*-LAT observations. The Vela pulsar is extremely bright in γ -rays, and its continuous observations by the LAT since the beginning of the mission enables us to directly construct regular times of arrival (TOAs) that are then used to generate a precise pulsar ephemeris (Ray et al. 2011).

The Vela pulsar experienced a glitch, i.e., a large jump in rotational frequency, near MJD 55428. To avoid any contamination from the Vela pulsar in the analysis of its PWN, data between MJD 55407 and MJD 55429 were excluded from the data set, and two timing solutions (pre- and post-glitch) were used to phase-fold the γ -ray photons. The pre-glitch ephemeris was built using 198 TOAs covering the period from the beginning of the science phase of the *Fermi* mission (2008 August 4) to the glitch, while the post-glitch timing solution was built using 197 TOAs from the glitch to 2012 August 4. For both timing solutions, we fit the γ -ray TOAs to the pulsar rotation frequency and first five derivatives. The fit further includes 10 harmonically related sinusoids, using the FITWAVES option in the TEMPO2 package (Hobbs et al. 2006), to flatten the timing noise. The post-fit rms is $91.3 \mu\text{s}$ and $97.7 \mu\text{s}$ (i.e., 0.1% of the pulsar phase) for the pre- and post-glitch ephemeris, respectively. These timing solutions will be made available through the Fermi Science Support Center (FSSC).⁸ We define phase 0 for the model based on the fiducial point from the radio timing observations, which is the peak of the radio pulse at 1.4 GHz.

Pulse phases were assigned to the LAT data using the *Fermi* plug-in provided by the LAT team and distributed with TEMPO2. Only γ -ray photons in the 0.8–1.0 pulse phase interval, corresponding to the off-pulse window, were selected and used for the spectral and morphological analysis presented in the following sections. Figure 1 shows the γ -ray light curve of the Vela pulsar obtained in the 0.1–300 GeV energy range using events in a 1° radius around the position of the Vela pulsar and the definition of the off-pulse window (blue dashed lines). It is worth noting that this phase interval was chosen to be narrower than the one used in the previous *Fermi*-LAT analysis to avoid any contamination from the Vela pulsar, which was estimated to be $\sim 6\%$ in the 0.7–0.8 phase interval (Abdo et al. 2010b).

4. ANALYSIS OF THE VELA-X PWN

The spatial and spectral analysis of the γ -ray data was performed using two different tools, *gtlike* and *pointlike*. *gtlike* is a maximum-likelihood method (Mattox et al. 1996) implemented in the Science Tools distributed by the FSSC. *pointlike* is an alternative binned likelihood technique, optimized for characterizing the extension of a source (unlike *gtlike*), which has been extensively tested against *gtlike* (Kerr, 2011; Lande et al. 2012). These tools fit a model of the region, including sources, residual cosmic-ray, extragalactic and Galactic backgrounds, to the data.

In the following analysis, the Galactic diffuse emission is modeled using the standard model *gal_2yearp7v6_v0.fits*.

⁸ Pulsar timing models:

<http://fermi.gsfc.nasa.gov/ssc/data/access/lat/ephems/>

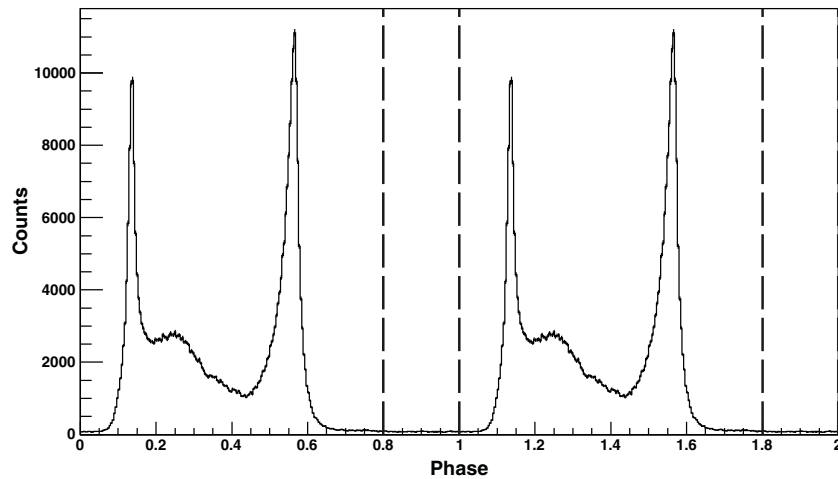


Figure 1. Gamma-ray light curve of the Vela pulsar in the 0.1–300 GeV energy range using events in a 1° radius around the Vela pulsar position. The binning of the light curve is 0.004 in pulsar phase. The main peak of the radio pulse seen at 1.4 GHz is at phase 0. Two cycles are shown. The off-pulse window (shown by dashed blue lines) used for the analysis of the Vela-X PWN was defined between 0.8 and 1.0 of the pulsar phase.

The residual charged particles and extragalactic radiation are described by a single isotropic component with a spectral shape described by the file *iso_p7v6source.txt*. The models and their detailed description are released by the LAT Collaboration.⁹

Sources within 10° of the Vela pulsar are extracted from the Second *Fermi*-LAT Catalog (Nolan et al. 2012) and used in the likelihood fit. The nearby bright and extended SNRs Puppis A and Vela Jr are modeled with their best-fit models, i.e., a uniform disk of radius $0^\circ:38$ for Puppis A (Hewitt et al. 2012) and the template of the TeV emission as seen with H.E.S.S. for Vela Jr (Tanaka et al. 2011). The spectral parameters of sources closer than 3° to Vela-X are left free, while the parameters of all other sources are fixed at the values from Nolan et al. (2012). Due to the longer integration time of our analysis (48 months versus 24 months in the catalog) and the overwhelming brightness of the Vela pulsar in the full phase interval, the appearance of additional sources in our region of interest is expected. These sources, denoted with the identifiers BckgA and BckgB, were also considered in the analysis of SNR Puppis A and were fit at the following positions: BckgA at $\alpha(\text{J2000}) = 125^\circ:77$, $\delta(\text{J2000}) = -42^\circ:17$ with a 68% error radius of $0^\circ:06$; BckgB at $\alpha(\text{J2000}) = 128^\circ:14$, $\delta(\text{J2000}) = -43^\circ:39$ with a 68% error radius of $0^\circ:05$. More details on these sources are available in Hewitt et al. (2012).

4.1. Morphology

Previous analysis of the Vela-X PWN using 11 months of *Fermi*-LAT data have shown that the source is significantly extended above 0.8 GeV, with an extension of $\sigma_{\text{Disk}} = 0^\circ:88 \pm 0^\circ:12$ assuming a uniform disk (hereafter labeled “*Disk11m*”; Abdo et al. 2010b).

The increasing statistics and the improvement of the IRFs with respect to Abdo et al. (2010b) allow a more detailed study of the source and the use of a lower energy threshold of 0.3 GeV.

To study the morphology of an extended source, a major requirement is to have the best possible angular resolution. Consequently, we restrict the LAT data set to *front* events only,

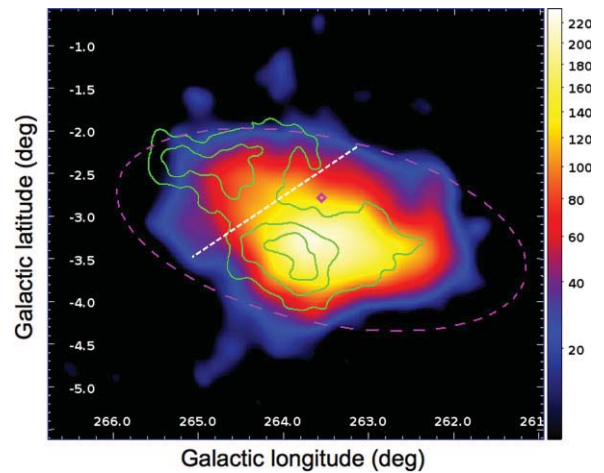


Figure 2. Gamma-ray TS map of the Vela-X PWN in the 0.3–100 GeV energy range (using *front* events only, Galactic coordinates). The 61 GHz *WMAP* radio contours (0.80, 0.95, and 1.1 mK) are overlaid for comparison. The dashed white line shows the division of the radio template in two halves. The dashed magenta ellipse shows the best-fit morphological model, i.e., the elliptical Gaussian (99% containment). The position of the Vela pulsar is marked with a magenta diamond. The color-coding is represented on a square-root scale.

(A color version of this figure is available in the online journal.)

i.e., events that convert in the thin layers of the tracker, which benefit from higher angular resolution¹⁰ (Atwood et al. 2009).

Figure 2 presents the *Fermi*-LAT Test Statistic (TS) map of γ -ray emission around the Vela-X PWN above 0.3 GeV using *front* events only. The TS is defined as twice the difference between the likelihood L_1 obtained by fitting a source model plus the background model to the data, and the likelihood L_0 obtained by fitting the background model only: $\text{TS} = 2(\log L_1 - \log L_0)$. This skymap contains the TS value for a point source at each map location, thus giving a measure of the statistical significance for the detection of a γ -ray source in excess of the background. The diffuse Galactic and isotropic emission, as well as nearby sources are included in the background model and subtracted from the map.

⁹ These models are available at <http://fermi.gsfc.nasa.gov/ssc/data/access/lat/BackgroundModels.html>

¹⁰ For more information, please see the *Fermi*-LAT performance page: http://www.slac.stanford.edu/exp/glast/groups/canda/lat_Performance.htm

Table 1
Centroid and Extension Fits to the LAT Data for Vela-X Using `pointlike` for *front* Events above 0.3 GeV

Spatial Model	R.A. ($^{\circ}$)	Decl. ($^{\circ}$)	σ_1 ($^{\circ}$)	σ_2 ($^{\circ}$)	P.A. ($^{\circ}$)	$2(\log L_1 - \log L_0)^a$	Add. d.o.f. ^b
Point source	128.40	-45.54				237	4
Gaussian	128.49	-45.38	0.80 ± 0.05			453	5
Disk	128.46	-45.37	1.27 ± 0.10			427	5
Elliptical Gauss	128.40	-45.40	0.46 ± 0.05	1.04 ± 0.08	40.3 ± 0.3	481	7
Elliptical disk	128.53	-45.38	0.85 ± 0.05	1.77 ± 0.09	39.6 ± 4.2	476	7
H.E.S.S.						316	2
Radio						431	2
Southern radio wing						401	2
Split radio model						447	4

Notes.

^a L_1 and L_0 are defined as the likelihood values corresponding to the fit of the spatial model described in the first column plus the background model and the fit of the background model only (null hypothesis).

^b Add. d.o.f.: additional degrees of freedom.

We used `pointlike` to measure the source extension using five different spatial hypotheses: a point source, a uniform disk hypothesis, a Gaussian distribution, an elliptical Gaussian distribution, and an elliptical disk (Lande et al. 2012), assuming a power-law spectrum. The results of the extension fits and the improvement of the TS when using spatially extended models are summarized in the first half of Table 1, along with the number of additional degrees of freedom with respect to the null hypothesis.

The improvement of the likelihood fit between a Gaussian distribution and the point-source hypothesis¹¹ (difference in TS of 216, which corresponds to an improvement at a $\sim 15\sigma$ level) supports a significantly extended source. The best-fit model in the 0.3–100 GeV energy range is obtained for an elliptical Gaussian distribution. This best-fit model represents a 5σ improvement with respect to a symmetric Gaussian distribution ($\Delta TS = 28$ for two additional degrees of freedom), which means that the source is also significantly elongated. The best-fit center of gravity of the emission region is (R.A., decl.) = ($128^{\circ}40 \pm 0^{\circ}05$, $-45^{\circ}40 \pm 0^{\circ}05$). The best-fit width along the major axis is $1^{\circ}04 \pm 0^{\circ}09$, while the best-fit intrinsic width along the minor axis is $0^{\circ}46 \pm 0^{\circ}05$. The major axis of the fitted distribution is at a position angle (P.A.) of $40^{\circ}3 \pm 4^{\circ}0$.

We also examined the correlation of the γ -ray emission from Vela-X with multi-wavelength observations of this PWN using `pointlike`. We compared the TS obtained with the best-fit model, i.e., the elliptical Gaussian distribution, with the TS obtained using the templates derived from *Wilkinson Microwave Anisotropy Probe* (WMAP; 61 GHz radio image, shown by green contours in Figure 2) and H.E.S.S. observations. For each analysis, a power-law spectrum was assumed. The resulting TS values, which are equivalent to $2\Delta(\log(L))$, are summarized in the second half of Table 1. When comparing the results obtained by modeling the Fermi-LAT emission with multi-wavelength templates, using the H.E.S.S. template significantly decreases the value of the likelihood with respect to the WMAP template, as noted in the first publication reporting the Fermi-LAT detection of the Vela-X PWN (Abdo et al. 2010b). However, we still observe a good correlation between the radio and the Fermi-LAT observations. We also divided the radio template into two halves, as indicated in Figure 2, to look for an energy-dependent

morphological behavior. The split radio model provides an improvement at $\sim 3.6\sigma$ and $\sim 6.5\sigma$ levels with respect to the single radio template and the southern radio wing model, respectively, and is also confirmed by the spectral analysis (see Section 4.2).

The multi-wavelength templates and the analytical models cannot be compared directly since the models are not nested. In the following analysis, we decided to use the best geometrical morphology implemented in `pointlike`, namely the elliptical Gaussian distribution.

Figure 3 presents the Fermi-LAT TS maps of γ -ray emission around the Vela-X PWN in two energy bands (0.3–1 GeV, 1–100.0 GeV) using *front* events only. Radio and TeV contours have been overlaid for comparison. We attempted to characterize the energy-dependent shape of the PWN by estimating the source extension in these energy intervals. The centroids and extensions in the different energy ranges are summarized in Table 2. From Figure 3 we note that the emission in the “northern wing” (defined with respect to the Galactic coordinates) of the radio emission is bright in the lower energy band and becomes faint above 1 GeV, which might be an indication of a softer spectrum than the “southern wing.”

It is worth noting that here we report for the first time the detection of γ -ray emission from the northern wing of the Vela-X PWN. This detection is clearly visible in the TS map presented in Figure 4, in which the southern radio wing was included in the background model. Table 1 shows that the log-likelihood of the fit is significantly improved by using the split radio templates instead of the southern radio wing only. The discovery was enabled by the low-energy threshold (0.3 GeV) now considered in this analysis. In addition, the extension and position of the southern wing are in full agreement with the results of the morphological fit performed above 0.8 GeV and reported in the first Fermi-LAT paper on Vela-X (Abdo et al. 2010b).

4.2. Spectrum

The following spectral analyses are performed with `gtlike` using *front* and *back* events between 0.2 and 100 GeV. We used the best morphological model from Table 1, i.e., the elliptical Gaussian distribution, to represent the γ -ray emission observed by the LAT, as discussed in Section 4.1.

Assuming this spatial shape, the γ -ray source observed by the LAT is detected with a TS of 940 above 0.2 GeV. The spectrum

¹¹ The formula used to derive the significance of an improvement when comparing two different spatial models with different numbers of degrees of freedom is extracted from Particle Data Group (Beringer et al. 2012).

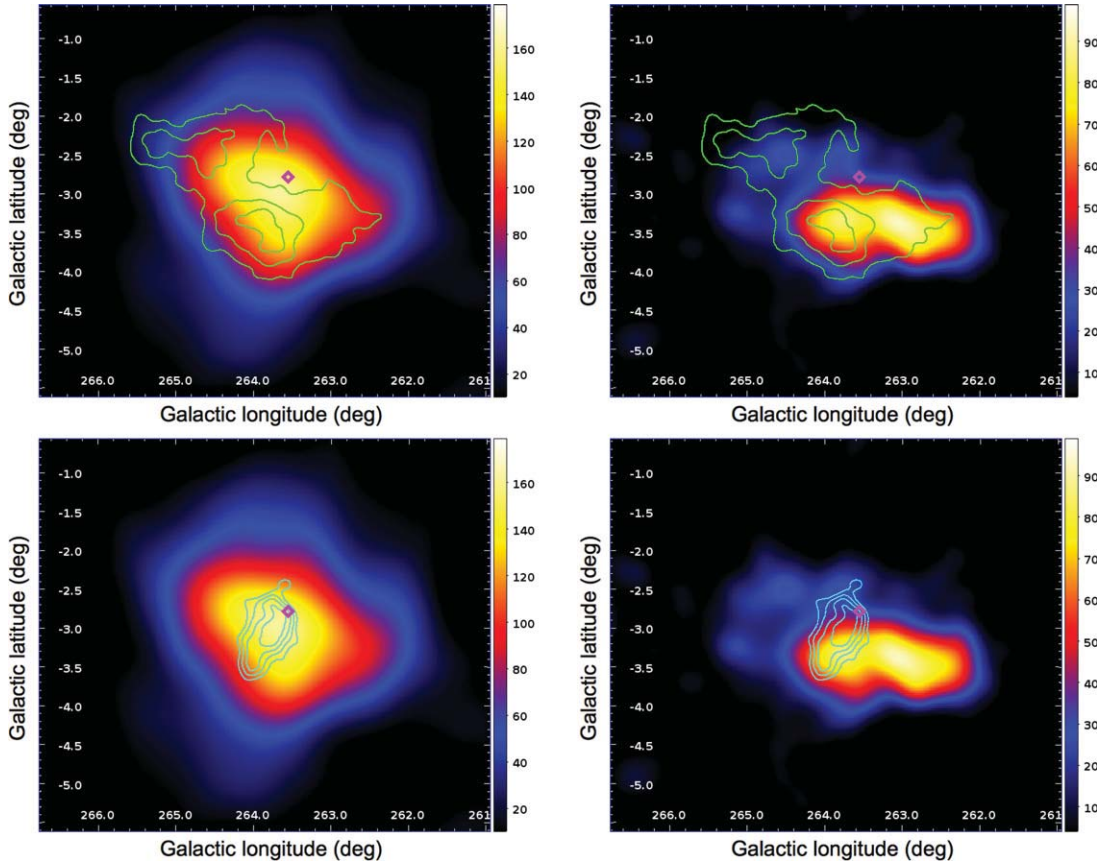


Figure 3. *Fermi*-LAT TS maps of the Vela-X PWN in the 0.3–1.0 (left) and 1.0–100.0 GeV (right) energy ranges, (using *front* events only, Galactic coordinates). The contours of the WMAP 61 GHz radio (in green, top row) and TeV emission (in light blue, bottom row Aharonian et al. 2006) are overlaid for comparison. The position of the Vela pulsar is marked with a magenta diamond.

(A color version of this figure is available in the online journal.)

Table 2

Centroid and Extension Fits to the LAT Data for Vela-X using *pointlike* for *front* Events, Assuming an Elliptical Gaussian Distribution

Energy Range	R.A. ($^{\circ}$)	Decl. ($^{\circ}$)	σ_1 ($^{\circ}$)	σ_2 ($^{\circ}$)	P.A. ($^{\circ}$)	$2(\log(L_1) - \log(L_0))$
0.3–100 GeV	128.40 ± 0.06	-45.40 ± 0.05	0.46 ± 0.05	1.04 ± 0.09	40.3 ± 4.0	481
0.3–1.0 GeV	128.75 ± 0.11	-45.33 ± 0.12	0.88 ± 0.15	1.02 ± 0.16	44.4 ± 13.4	216
1.0–100.0 GeV	128.26 ± 0.06	-45.39 ± 0.06	0.43 ± 0.06	1.07 ± 0.11	44.3 ± 1.9	291

of Vela-X above 0.2 GeV is presented in Figure 5. It is well described by a smoothly broken power law:

$$F(E) = \frac{dN}{dE} = N_0 \left(\frac{E}{E_0} \right)^{-\Gamma_1} \left(1 + \left(\frac{E}{E_b} \right)^{\frac{\Gamma_1 - \Gamma_2}{\beta}} \right)^{-\beta}, \quad (1)$$

where $\Gamma_1 = 1.83 \pm 0.07 \pm 0.27$, $\Gamma_2 = 2.88 \pm 0.21 \pm 0.06$ are the spectral indices below and above the break energy $E_b = 2.1 \pm 0.5 \pm 0.5$ GeV. The parameter β is fixed to the value 0.2 as in standard *Fermi*-LAT analyses (e.g., Buehler et al. 2012). The first error is statistical, while the second represents our estimate of systematic effects as discussed below. The integrated flux renormalized to the total phase above 0.2 GeV is $(1.83 \pm 0.08 \pm 0.25) \times 10^{-7} \text{ cm}^{-2} \text{ s}^{-1}$. This spectral model is favored over the simple power law and an exponential cutoff power law at 6.6σ and 2.7σ levels, respectively. This is in agreement with results obtained independently using *pointlike*. Similar results are obtained with the radio template, as can be seen in Table 3.

The *Fermi*-LAT spectral points shown in Figure 5 were obtained by dividing the 0.2–100 GeV range into 10 logarithmically spaced energy bins and performing a maximum likelihood spectral analysis to estimate the photon flux in each interval, assuming a power-law shape with fixed photon index $\Gamma = 2$ for the source. The normalizations of the diffuse Galactic and isotropic emission were left free in each energy bin. A 99.73% C.L. upper limit is computed when the statistical significance is lower than 3σ . Bins at the highest energies corresponding to upper limits were combined.

Four different systematic uncertainties can affect the LAT flux estimation: uncertainties in the Galactic diffuse background, in the morphology of the LAT source, in the effective area, and in the energy dispersion. The fourth one is relatively small ($\leq 10\%$) and has been neglected in this study. The main systematic at low energy is due to the uncertainty in the Galactic diffuse emission since Vela-X is located only $\sim 3^{\circ}$ from the Galactic plane. Different versions of the Galactic diffuse emission, generated by GALPROP (Strong et al. 2004), were used to estimate this error. The observed γ -ray intensity of nearby source-free regions

Table 3
Best Spectral Fit Values Obtained with `gtlike` Using Different Templates for Vela-X above 0.2 GeV

Spatial Model	Flux (10^{-7} photons cm^{-2} s^{-1}) ^a	Photon Index Γ_1	Photon Index Γ_2	Break Energy E_b	TS
Elliptical Gaussian	$1.83 \pm 0.08 \pm 0.25$	$1.83 \pm 0.07 \pm 0.27$	$2.87 \pm 0.21 \pm 0.06$	$2.1 \pm 0.5 \pm 0.5$	940
Radio	$1.73 \pm 0.08 \pm 0.22$	$1.88 \pm 0.08 \pm 0.27$	$2.89 \pm 0.23 \pm 0.05$	$2.0 \pm 0.5 \pm 0.5$	897
Split radio templates :					
Northern wing ^b	$0.64 \pm 0.08 \pm 0.14$	$2.25 \pm 0.07 \pm 0.20$...	–	116
Southern wing	$1.12 \pm 0.08 \pm 0.09$	$1.81 \pm 0.10 \pm 0.24$	$2.90 \pm 0.25 \pm 0.07$	$2.1 \pm 0.5 \pm 0.6$	606
<i>Disk11m</i> ^c	1.58 ± 0.07	2.24 ± 0.04	...	–	770
<i>Disk11m</i> ^c	1.50 ± 0.07	1.96 ± 0.07	3.01 ± 0.30	2.0 ± 0.3	804

Notes.

The First and Second Errors Denote Statistical and Systematic Errors, Respectively.

^a Fluxes are estimated above 0.2 GeV and renormalized to the total phase interval. The spectral parameter β was fixed to the value 0.2.

^b The spectral parameters of the northern wing were obtained after two iterations, as explained in the text.

^c The “*Disk11m*” model here refers to the best morphological fit obtained with 11 months of *Fermi*-LAT data (Abdo et al. 2010b).

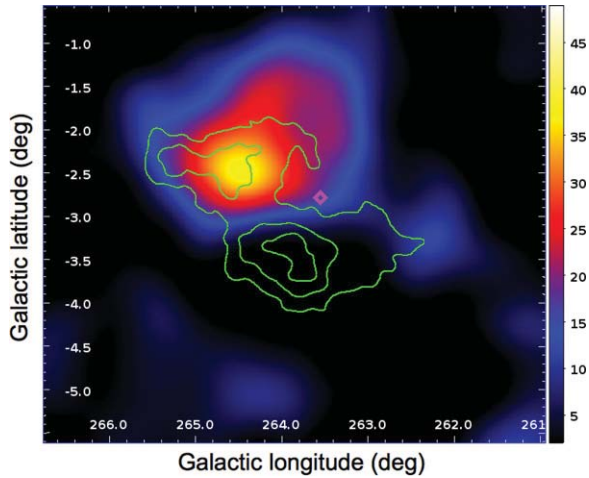


Figure 4. *Fermi*-LAT TS map of the Vela-X PWN in the 0.3–1.0 energy range (using *front* events only, Galactic coordinates). The southern wing of the radio emission has been included in the background model. Significant γ -ray emission coincident with the northern wing of the radio emission is detected by the *Fermi*-LAT. The contours of the *WMAP* 61 GHz radio (in green) are overlaid for comparison. The position of the Vela pulsar is marked with a magenta diamond. (A color version of this figure is available in the online journal.)

on the Galactic plane is compared with the intensity expected from the Galactic diffuse models. We adopted the strategy described in Abdo et al. (2010c) to estimate the expected intensity of the Galactic diffuse emission for different models. The difference, namely the local departure from the best-fit diffuse model, is found to be $\leq 6\%$. By changing the normalization of the Galactic diffuse model artificially by $\pm 6\%$, we estimate the systematic error on the integrated flux and on the spectral index. The second systematic is related to the morphology of the LAT source. The fact that we do not know the true γ -ray morphology introduces another source of error that becomes significant when the size of the source is larger than the point spread function. Different spatial shapes have been used to estimate this systematic error: a disk, a Gaussian distribution, and the radio template. The third uncertainty, common to every source analyzed with the LAT data, is due to the uncertainties in the effective area. This systematic is estimated by using modified IRFs whose effective area bracket that of our nominal IRF. These “biased” IRFs are defined by envelopes above and below the nominal dependence of the effective area with energy by linearly connecting differences of (10%, 5%, 10%) at $\log(E)$ of (2, 2.75, 4), respectively. We combine these various errors in quadrature to obtain our best estimate of the total systematic

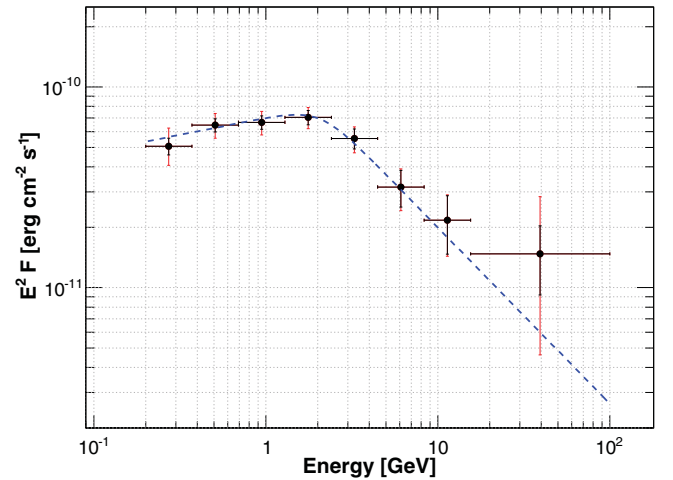


Figure 5. Gamma-ray spectra of the Vela-X PWN, using the elliptical Gaussian spatial model. The blue dashed line shows the fit of a smoothly broken power law to the overall spectrum derived from all of the data with energy above 0.2 GeV. The data points (crosses) indicate the fluxes measured in each of the 10 energy bins indicated by the extent of their horizontal lines. The statistical errors are shown in black, while the red lines take into account both the statistical and systematic errors as discussed in Section 4.2. A 99.73% C.L. upper limit is computed when the statistical significance is lower than 3σ . (A color version of this figure is available in the online journal.)

error at each energy and propagate them through to the fit model parameters.

Table 3 summarizes the obtained fluxes and spectral indices for each of the spatial templates described in Table 1.

Using the elliptical Gaussian distribution and the smoothly broken power law and assuming a distance of $D = 290$ pc, the γ -ray luminosity of Vela-X above 0.2 GeV is $L_\gamma \approx 2.4 \times 10^{33} (D/290 \text{ pc})^2 \text{ erg s}^{-1}$, yielding a γ -ray efficiency of $\eta = L_\gamma / \dot{E} = 0.03\%$ of the spin-down power of the Vela pulsar.

We attempted to characterize the energy-dependent morphology of the Vela-X PWN by fitting the spectra associated with each of the split radio templates with independent spectral models. The results are summarized in Table 3. The northern wing is well modeled with a simple power law of index $2.25 \pm 0.07 \pm 0.20$, while the southern wing is better described by a smoothly broken power law. The corresponding spectral parameters are the following: $\Gamma_1 = 1.81 \pm 0.10 \pm 0.24$ and $\Gamma_2 = 2.90 \pm 0.25 \pm 0.07$, with a break energy of $E_b = 2.1 \pm 0.5 \pm 0.6$ GeV. Because of a potential interdependence of the wing spectral fits, the northern parameters were obtained after two iterations. In

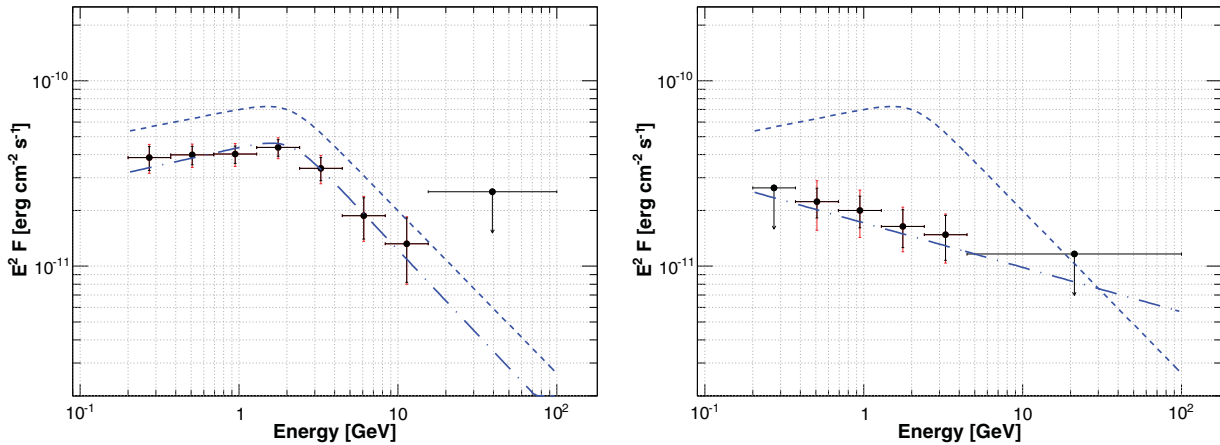


Figure 6. Gamma-ray spectra of the two components of the Vela-X PWN, as defined in Section 4.1. The blue dot-dashed line shows the best fit of the overall spectrum derived from all of the data with energy above 0.2 GeV. The left and right images correspond to the southern and northern wings, respectively. The spectrum obtained with the single radio template is indicated by a blue dashed line (as shown in Figure 5). The plot conventions are similar to Figure 5.

(A color version of this figure is available in the online journal.)

a first step, both wings were fitted simultaneously. The northern wing being much fainter than the southern one, the spectral parameters of the northern wing were readjusted in the second step, using fixed parameters for the southern wing. Both iterations yield consistent results within statistical errors. However, the fit and spectral points obtained in the second step for the northern wing are much more in agreement with each other. It is worth noting that the flux of the northern wing is approximately half of the one in the southern wing. However the northern wing is located closer to the Galactic plane (i.e., in a region with a larger contribution from the Galactic diffuse background), which renders the emission from this wing less than half as significant as than the southern wing. The improvement for the split radio model with respect to the single radio template is at $\sim 4\sigma$ level, which is consistent with the fact that the integral fluxes of the two radio wings are significantly different (see Table 3). Figure 6 (left and right) presents the spectra of the two regions modeled with the two split templates. Interestingly, this analysis shows that below ~ 2 GeV, the northern wing has a softer spectrum by an index of ~ 0.5 with respect to the southern wing, confirming the first indications given by the TS maps (see Figure 3). However, it should be noted that the steep spectrum of the northern wing is mainly constrained by the upper limits at HE. In this context, the likelihood of the fit is improved by only 2.5σ when using a free power-law model instead of a broken power law with fixed energy break and spectral indices (frozen at the values obtained for the southern wing). More statistics are therefore needed to confirm spectral differences between the northern and southern regions.

The careful reader may note that the best spectral fit of 4 yr of *Fermi*-LAT data (this paper) is obtained with a smoothly broken power law, while the fit of the 11 months of data yielded a simple power law of index $\Gamma \sim 2.4 \pm 0.1$ and a weaker flux as presented in Abdo et al. (2010b). These differences arise from the three main improvements (described below) made in this new analysis.

First, a larger data set now enables us to spatially model the Vela-X γ -ray emission with an elliptical Gaussian distribution, i.e., a more elaborate morphology than the “*Disk11m*” model considered in the previous publication. The smaller extension of the *Disk11m* with respect to the elliptical Gaussian distribution above 0.2 GeV therefore yields a fainter flux integrated over 0.2 GeV. For comparison, the spectral parameters obtained by

fitting the 4 yr data set with a power law and a smoothly broken power law using the *Disk11m* spatial model are included in Table 3.

Second, the increased statistics now allow a significant detection of a spectral break at ~ 2.0 GeV in the γ -ray domain, which was not possible with only 11 months of data. Using *Disk11m*, the smoothly broken power law is preferred to the simple power law at 5.3σ level.

Finally, using the *Disk11m* model, the harder spectrum obtained with the 4 yr data set (spectral index of $\Gamma = 2.24 \pm 0.04$ for a power law, see the first row labeled “*Disk11m*” in Table 3) with respect to the 11 month data set (which yielded a spectral index of $\Gamma = 2.4 \pm 0.1$) presented in Abdo et al. (2010b) likely arises from the slight contamination of the 11 month data set by the Vela pulsar at low energies (below 1 GeV), which was estimated to be $\sim 6\%$ of the Vela-X flux. Defining the off-pulse window as 20% of the pulsar phase (instead of 30% in Abdo et al. 2010b) ensures that we do not suffer contamination from the Vela pulsar in the new analysis.

4.3. Multi-wavelength Data

Spectral measurements at different frequencies may help to better understand the origin of the emission observed from a source via the modeling of its spectral energy distribution. Considering the strong connection between the radio domain and the GeV energy range emphasized in Abdo et al. (2010b), we examined in particular the data obtained in radio in this complex region.

Seven-year all-sky data of the *WMAP* were used to extract the spectrum of the Vela-X PWN at high radio frequencies. Five bands were analyzed, with effective central frequencies of 23, 33, 41, 61, and 94 GHz (Jarosik et al. 2011). Figure 7 represents the composite radio sky map in the Vela-X field of view. This image also shows evidence for a contaminating high-frequency component superimposed on the PWN, especially on the western side of the northern wing, for Galactic coordinates $(l, b) \sim (265^\circ 8, -2^\circ 5)$.

We extracted the radio spectral measurements using the regions delimited with the white ellipses and red circles for the source and background estimation, respectively. The radio spectral points obtained within the southern and northern regions in the five frequencies covered by *WMAP* are summarized in

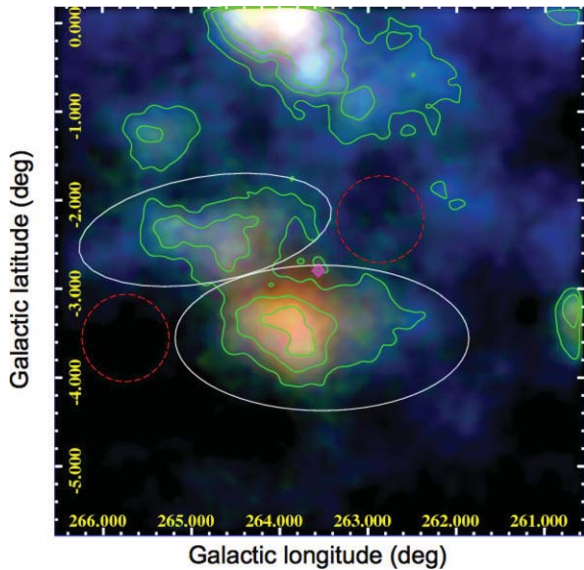


Figure 7. Composite radio sky map obtained from *WMAP* data in Galactic coordinates (red: 41 GHz, green: 61 GHz, blue: 94 GHz) smoothed with a $3'6$ Gaussian kernel. The magenta diamond shows the pulsar position. The extraction regions delimited with the white solid ellipses and the dashed red circles are used for the flux measurements for the source and the background, respectively. The 61 GHz *WMAP* radio contours (0.80, 0.95, and 1.1 mK) are overlaid as green solid lines.

(A color version of this figure is available in the online journal.)

Table 4

WMAP Spectral Points Corresponding to the Southern and Northern Regions

Band	Frequency (GHz)	Flux ($\times 10^{11}$ erg cm $^{-2}$ s $^{-1}$)	
		Southern Region	Northern Region
<i>K</i>	23	1.53 ± 0.26	0.75 ± 0.16
<i>Ka</i>	33	1.72 ± 0.28	0.88 ± 0.18
<i>Q</i>	40	1.76 ± 0.28	0.96 ± 0.18
<i>V</i>	60	2.29 ± 0.55	1.58 ± 0.35
<i>W</i>	93	4.02 ± 2.20	4.14 ± 1.42

Table 4 and represented in Figure 8. When excluding the highest frequency spectral point (which may be contaminated as shown in Figure 7), the fluxes in the two regions are well modeled with power laws $S_i \propto \nu^{-\alpha_i}$ (with $i = S, N$ for the south and north, respectively) of indices $\alpha_S = 0.76 \pm 0.15$ and $\alpha_N = 0.41 \pm 0.08$. Given the contamination noted above, this radio slope difference between the two wings may not be significant. Additional data, e.g., from *Planck*, and especially measurements above 40 GHz, are required to confirm this result.

To better constrain the physical parameters related to the PWN and its environment, we will use the above described spectral measurements in the following section. A low-frequency (0.4 GHz) spectral point is extracted from Haslam et al. (1982) and will be used as an upper limit on the flux in each wing of the radio emission.

5. DISCUSSION

5.1. Constraining the Magnetic Field in the Halo Extended Region

Determining the mechanism responsible for γ -ray emission is crucial in order to measure the underlying relativistic particle population accelerated in a PWN. This new analysis confirms the excellent correlation between the GeV and the radio mor-

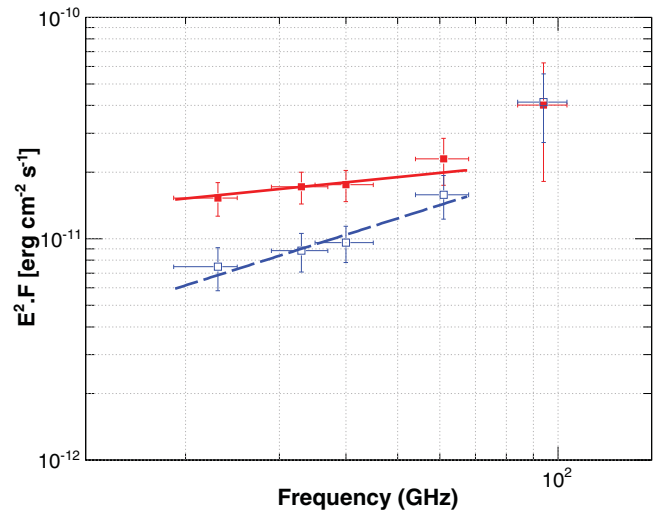


Figure 8. Radio spectrum of the Vela-X PWN in the southern (red, full squares) and northern (blue, open squares) regions. The solid red and long dashed blue lines represent the best fit obtained in the 19–70 GHz frequency range for the southern and northern wings, respectively.

(A color version of this figure is available in the online journal.)

Table 5

Values of the Parameters Assumed for the Modeling

Parameters	Value
Spectral index γ	1.8
Age (kyr)	11
Spin-down power \dot{E} (erg s $^{-1}$)	6.9×10^{36}
Pulsar braking index n	3.0

phologies, showing that the γ -ray emission extends well outside the narrow cocoon detected in X-rays and VHE.

In a first step, we attempted to reproduce the multi-wavelength spectral energy distributions of the southern and northern wings of Vela-X without taking into account the emissions in the cocoon (detected in X-rays and TeV) which could be produced by a separate electron population, as explained in Abdo et al. (2010b). The objective is to constrain the total energy injected in the form of electrons in the halo as well as the mean value of the magnetic field in this extended region. For this purpose, we used a one-zone model similar to the one described in Grondin et al. (2011). The hadronic scenario, according to which the VHE emission is produced by proton–proton interactions and neutral pion decays, was proposed by Horns et al. (2006) but seems to be disfavored because of the large particle density required with respect to the density derived from X-ray observations (LaMassa et al. 2008). Therefore, it will be disregarded in the following. The spectral differences between the northern and the southern wing being marginal with the current statistics of the *WMAP* and *Fermi*-LAT data, we did not try to reproduce this effect in the following scenario. In addition, due to the contamination visible at high frequencies in the *WMAP* data, we did not try to fit the spectral point at 94 GHz.

We assume the same leptonic spectrum injected in each region. The *WMAP* spectral index of ~ 0.4 in the southern region (which is the less contaminated) requires a particle index of $\gamma \sim 0.4 \times 2 + 1 \approx 1.8$, kept fixed in our model (see Table 5). In both regions, the leptonic spectrum injected shows an energy cutoff at the highest energy which is fitted and constrained by the observational data.

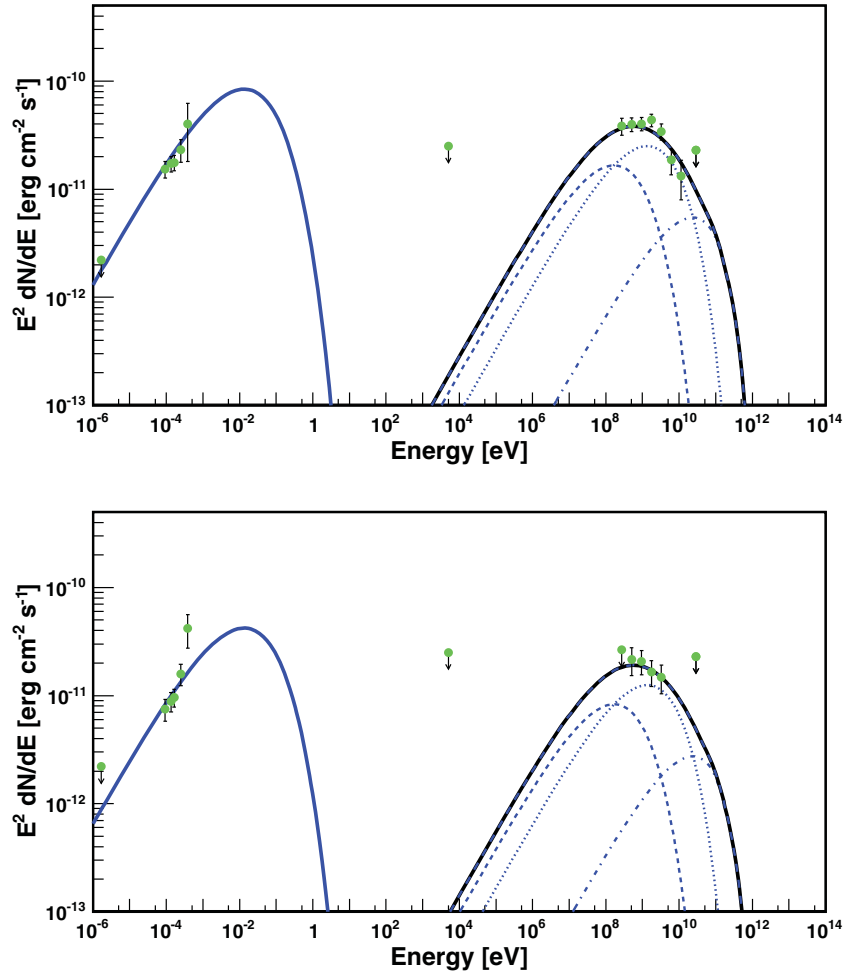


Figure 9. Spectral energy distributions of the southern (top) and northern (bottom) wings from radio to γ -rays. *WMAP* and *Fermi*-LAT spectral points (this paper) are represented with green points. The *ROSAT* upper limit (Abdo et al. 2010b) is also shown. The low-frequency radio upper limit is derived from Haslam et al. (1982). The dashed, dotted, and dot-dashed lines represent the inverse Compton components from scattering on the CMB, dust emission, and starlight, respectively. The sum of the three γ -ray components is shown as a solid curve.

(A color version of this figure is available in the online journal.)

Electrons suffer energy losses due to ionization, bremsstrahlung, synchrotron processes, and inverse Compton (IC) scattering. Escape outside the halo is also taken into account assuming Bohm diffusion. The modification of the electron spectral distribution due to such losses is determined following Aharonian et al. (1997). The electron population is evolved over the estimated lifetime of the pulsar (11 kyr). Here we fix the pulsar braking index to the canonical value of $n = 3.0$. The magnetic field and spin-down power of the pulsar are assumed to remain constant throughout the age of the system and do not depend on the size of the PWN. Neither the interaction of the reverse shock nor the diffusion of the leptons within the PWN are modeled since there are not enough observables to sufficiently constrain their corresponding parameters. In this context, this phenomenological model is used to reproduce the multi-wavelength data assuming that the Vela pulsar is the only source of energy.

The IC photon field includes the cosmic microwave background (CMB), far-infrared from the dust (IR; temperature of 25 K, density of 0.44 eV cm^{-3}), and starlight (optical; temperature of 7500 K, density of 0.44 eV cm^{-3}), reasonable for the locale of Vela-X (de Jager et al. 2008). We assume a distance of $D = 290 \text{ pc}$ and a size for each region (i.e., the northern and southern wings) of 10 pc.

Table 6
Best-fit Parameters for the Southern and Northern Wings

Parameters	Southern Wing	Northern Wing
Magnetic field B (μG)	4.9 ± 0.8	
Cutoff energy (GeV)	145 ± 30	
Fraction of spin-down power η (%)	26 ± 5	13 ± 2
Total energy injected to leptons ($\times 10^{47} \text{ erg}$)	6.2 ± 1.2	3.1 ± 0.5

All in all, our simple one-zone model has four free parameters adjusted to reproduce the photon spectral energy distribution as seen in radio (Haslam et al. 1982; this work) and γ -rays (this work) in both regions: the magnetic field B in the halo, the exponential cutoff energy (which are both assumed to be the same in the northern and southern regions), and the fraction η of the pulsar spin-down power injected to particles in each region. The best fit, obtained by minimizing the χ^2 statistic between model and data points, is shown in Figure 9 (top and bottom). As can be seen in this figure, a simple power-law injection model can reasonably well reproduce the multi-wavelength data of the two wings. The best-fit parameters are summarized in Table 6. Model fitting is achieved by minimizing the χ^2 between model and data using the simplex method

described in Nelder & Mead, (1965). This algorithm is included within the ROOT framework provided by CERN.¹² For each ensemble of N variable parameters, we evolve the system over the pulsar lifetime and calculate the χ^2 between model curves and flux data points. The simplex routine subsequently varies the parameters of interest to minimize the fit statistic. We estimate parameter errors by using MINOS, which is designed to calculate the correct errors in all cases, especially when there are nonlinearities. The theory behind the method is described in Eadie et al. (1971). It is worth noting that $\sim 26\%$ and $\sim 13\%$ of the total energy injected by the pulsar (which represents 100% of the spin-down power injected in particles accounting for all losses during the lifetime of the system) is required to power the radio to γ -ray emission from the southern and northern wings, respectively. In addition, the total energy injected into leptons and the magnetic field derived are both in very good agreement with previous estimates (de Jager et al. 2008; Aharonian et al. 2006; Abdo et al. 2010b). The synchrotron/IC peak ratio of the cocoon implies a magnetic field of $4 \mu\text{G}$ with very small uncertainty, which can be compared to our value of $\sim 5 \mu\text{G}$ in the halo. Since no data are available to trace the synchrotron peak and better constrain the magnetic field in the halo, we cannot exclude similar values in the halo and in the cocoon.

5.2. Rapid Diffusion of Electrons?

The radio emission, arising from synchrotron radiation, traces the magnetic field distribution. On the other hand, in a leptonic scenario, the HE emission is produced via IC scattering and directly traces the underlying relativistic electron distribution. The new *Fermi*-LAT results together with the correlation between the radio and γ -ray data now provide direct evidence that low-energy electrons are present in the extended halo. The recent H.E.S.S. detection of TeV emission coincident with the extended radio halo (Abramowski et al. 2012) is additional evidence that electrons are present in this large structure. In addition to that, the above simple modeling provides further evidence that the magnetic fields in the halo and cocoon regions are not strongly different. In that case, the real puzzle is to understand the origin of the electrons present in the extended radio halo since significant emission is now detected by *Fermi*-LAT and H.E.S.S. up to $\sim 1^\circ$ from the Vela pulsar, i.e., ~ 10 pc from the powering pulsar.

A potential scenario was first proposed by Van Etten & Romani, (2011) to explain the large size of the PWN H.E.S.S. J1825–137: rapid diffusion of HE particles with $\tau_{\text{esc}} \sim 90(R/10 \text{ pc})^2(E_e/100 \text{ TeV})^{-1} \text{ yr}$ (where R and E_e are the radius of the PWN and the energy of the injected electrons, respectively) which is 1000 times faster than standard Bohm diffusion. This is in contradiction with the common assumption of toroidal magnetic fields with strong magnetic confinement. The authors argue that turbulence and mixing caused by the passage of the reverse shock might provide the necessary disruption to the magnetic field structure to allow particles to diffuse far more rapidly. More recently, this fast diffusion was invoked for Vela-X by Hinton et al. (2011) to interpret the steep *Fermi*-LAT spectrum and the absence of >100 GeV photons in the extended radio halo. Their best fit to the data yields a factor of 2000 enhancement over Bohm diffusion. In such a scenario, the γ -ray flux observed by *Fermi*-LAT at the outer realm of the Vela-X extended nebula would be produced by HE electrons that were injected when the pulsar was much younger.

However, their model does not produce any TeV emission at a large distance from the pulsar since HE electrons escape too fast. A way to solve this issue would be to inject two populations of electrons (as suggested earlier by Abdo et al. 2010b) and decrease the diffusion time so that 10 TeV photons can still be visible up to 1° (10 pc) from the powering pulsar in a magnetic field B of $5 \mu\text{G}$. Since the standard Bohm diffusion time scale is $\tau_{\text{diff}} \sim 34(R/1 \text{ pc})^2(E_e/10 \text{ TeV})^{-1}(B/10 \mu\text{G}) \text{ kyr}$ (Zhang et al. 2008), a diffusion only ~ 20 times faster than Bohm diffusion would be needed. It should be noted that this scenario should lead to spectral differences between the inner and the outer regions of the PWN due to radiative cooling of the electrons during their propagation, which is in contradiction with the recent H.E.S.S. results (Abramowski et al. 2012). Energy-dependent diffusive escape and stochastic reacceleration in the radio halo could explain the absence of spectral variations in the TeV regime but such complex modeling is out of the scope of our paper.

Another possibility would be that these electrons do not come from the Vela pulsar and are directly accelerated in this extended structure through stochastic acceleration due to turbulent magnetic fields in the outer PWN flow or in the surrounding SNR plasma, since there is no evidence of shocks in this region. Such second-order Fermi acceleration accounts well for the radio emission from SNRs (Scott & Chevalier, 1975). It provides an excess of accelerated electrons that will radiate through synchrotron and IC radiation as seen in radio by *WMAP* and γ -rays by *Fermi*-LAT. The maximum energy to which electrons can be accelerated by such mechanism depends highly on the level of turbulence, which is unknown. To reproduce the *Fermi*-LAT spectrum, a reasonable maximum energy of ~ 140 GeV is required. Obviously, in this case, the radio/*Fermi* halo would not be linked with the X-ray/TeV cocoon. The TeV extended halo, if related to the radio structure, would need a second component of accelerated electrons to reproduce the peaked γ -ray spectrum. Unfortunately, the comparison of the radio, GeV and TeV emissions is limited by the differences in resolution and sensitivity of the instruments involved. In particular, the current multi-wavelength observations do not allow conclusions to be drawn about whether the TeV and radio emissions arise from the exact same location.

6. CONCLUSION

Using four years of *Fermi*-LAT observations and a lower energy threshold for the morphological analysis than previously, we report, for the first time, the detection of γ -ray emission from the northern wing of the Vela-X PWN. The best-fit geometrical morphological model in the 0.3–100 GeV energy range is obtained for an elliptical Gaussian distribution. We also report the detection of a significant energy break at $E_b = 2.1 \pm 0.5$ GeV in the *Fermi*-LAT spectrum as well as a marginal spectral difference between the northern and the southern wings. *WMAP* data have also been used to characterize the synchrotron emission in the two wings of the radio halo. However, the *WMAP* image shows evidence for a contaminating high-frequency component superimposed on the PWN, especially on the northern wing, and the radio slope difference observed between the two wings may not be significant.

Further observations to characterize the radio and γ -ray spectra are required and will help understand the origin of the excess of low-energy electrons detected in these two wavelengths. High-frequency radio observations are clearly needed to spatially resolve the radio emission, especially above 60 GHz.

¹² ROOT: <http://root.cern.ch/>

Increased sensitivity with the continued observations by *Fermi*-LAT will also enable any spectral differences between the northern and southern regions to be firmly established. In addition, observations with H.E.S.S.-II will provide a better overlap with *Fermi*-LAT and therefore a direct link to verify if the TeV signal is related to the extended structure detected by *Fermi*. In addition, deeper observations with high sensitivity instruments such as *XMM-Newton* will help to better constrain the spectra and their potential spatial variations in the cocoon and halo in the X-ray domain. Despite a large sample of multi-wavelength data, Vela-X remains an excellent case to study and the future observations in radio and γ -rays will obviously provide new clues to understand the acceleration mechanisms taking place in this complex object, as well as new surprises.

The *Fermi*-LAT Collaboration acknowledges generous ongoing support from a number of agencies and institutes that have supported both the development and the operation of the LAT as well as scientific data analysis. These include the National Aeronautics and Space Administration and the Department of Energy in the United States; the Commissariat à l’Energie Atomique and the Centre National de la Recherche Scientifique/Institut National de Physique Nucléaire et de Physique des Particules in France; the Agenzia Spaziale Italiana and the Istituto Nazionale di Fisica Nucleare in Italy; the Ministry of Education, Culture, Sports, Science and Technology (MEXT), High Energy Accelerator Research Organization (KEK), and the Japan Aerospace Exploration Agency (JAXA) in Japan; and the K. A. Wallenberg Foundation, the Swedish Research Council, and the Swedish National Space Board in Sweden.

Additional support for science analysis during the operations phase is gratefully acknowledged from the Istituto Nazionale di Astrofisica in Italy and the Centre National d’Études Spatiales in France.

M.H.G. acknowledges support from the Alexander von Humboldt Foundation (Germany) and from the Centre National d’Études Spatiales (CNES, France). M.H.G. thanks Felix A. Aharonian and Patrick O. Slane for helpful comments and discussions.

REFERENCES

- Abdo, A., Ackermann, M., Ajello, M., et al. 2009a, *PhRvD*, **80**, 122004
 Abdo, A., Ackermann, M., Ajello, M., et al. 2010a, *ApJ*, **713**, 154
 Abdo, A., Ackermann, M., Ajello, M., et al. 2010b, *ApJ*, **713**, 146
 Abdo, A., Ackermann, M., Ajello, M., et al. 2010c, *ApJ*, **722**, 1303
 Abdo, A., Ackermann, M., Atwood, W. B., et al. 2009b, *ApJ*, **696**, 1084
 Abramowski, A., Acero, F., Aharonian, F., et al. 2012, *A&A*, **548**, A38
 Ackermann, M., Ajello, M., Albert, A., et al. 2012, *ApJS*, **203**, 4
 Aharonian, F. A., Akhperjanian, A. G., Bazer-Bachi, A. R., et al. 2006, *A&A*, **448**, L43
 Aharonian, F. A., Atoyan, A. M., & Kifune, T. 1997, *MNRAS*, **291**, 162
 Alvarez, H., Aparici, J., May, J., & Reich, P. 2001, *A&A*, **372**, 636
 Atwood, W. B., Abdo, A. A., Ackermann, M., et al. 2009, *ApJ*, **697**, 1071
 Beringer, J., Arguin, J.-F., Barnett, R. M., et al. 2012, *PhRvD*, **86**, 010001
 Buehler, R., Scargle, J. D., Blandford, R. D., et al. 2012, *ApJ*, **749**, 26
 Caraveo, P. A., De Luca, A., Mignani, R. P., & Bignami, G. F. 2001, *ApJ*, **561**, 930
 de Jager, O. C., Harding, A. K., & Strickman, M. S. 1996, *ApJ*, **460**, 729
 de Jager, O. C., Slane, P. O., & LaMassa, S. M. 2008, *ApJL*, **689**, L125
 Dodson, R., Legge, D., Reynolds, J. E., & McCulloch, P. M. 2003, *ApJ*, **596**, 1137
 Eadie, W. T., Drijard, D., James, F., Roos, M., & Sadoulet, B. 1971, *Statistical Methods in Experimental Physics* (Amsterdam: North-Holland), 204
 Fang, J., & Zhang, L. 2010, *A&A*, **515**, 20
 Gaensler, B. M., & Slane, P. O. 2006, *ARA&A*, **44**, 17
 Grondin, M.-H., Funk, S., Lemoine-Goumard, M., et al. 2011, *ApJ*, **738**, 42
 Haslam, C. G. T., Salter, C. J., Stoffel, H., & Wilson, W. E. 1982, *A&AS*, **47**, 1
 Hewitt, J., Grondin, M.-H., Lemoine-Goumard, M., Reposeur, T., et al. 2012, *ApJ*, **759**, 89
 Hinton, J., Funk, S., Parsons, R. D., & Ohm, S. 2011, *ApJL*, **743**, L7
 Helfand, D. J., Gotthelf, E. V., & Halpern, J. P. 2001, *ApJ*, **556**, 380
 Hobbs, G. B., Edwards, R. T., & Manchester, R. N. 2006, *MNRAS*, **369**, 655
 Horns, D., Aharonian, F., Santangelo, A., Hoffmann, A. I. D., & Masterson, C. 2006, *A&A*, **451**, L51
 Jarosik, N., Bennett, C. L., Dunkley, J., et al. 2011, *ApJS*, **192**, 14
 Kanbach, G., Arzoumanian, Z., Bertsch, D. L., et al. 1994, *A&A*, **289**, 855
 Kerr, M. 2011, PhD thesis, Univ. Washington
 LaMassa, S. M., Slane, P. O., & De Jager, O. C. 2008, *ApJL*, **689**, L121
 Lande, J., Ackermann, M., Allafort, A., et al. 2012, *ApJ*, **756**, 5
 Large, M. I., Vaughan, A. E., & Mills, B. Y. 1968, *Natur*, **220**, 340
 Markwardt, C. B., & Ögelman, H. 1995, *Natur*, **375**, 40
 Mattox, J. R., Bertsch, D. L., Chiang, J., et al. 1996, *ApJ*, **461**, 396
 Nelder, J. A., & Mead, R. 1965, *Comput. J.*, **7**, 308
 Nolan, P. L., Abdo, A. A., Ackermann, M., et al. 2012, *ApJS*, **199**, 31
 Ögelman, H., Finley, J. P., & Zimmerman, H. U. 1993, *Natur*, **361**, 136
 Pellizzoni, A., Trois, A., Tavani, M., et al. 2010, *Sci*, **327**, 663
 Ray, P. S., Kerr, M., Parent, D., et al. 2011, *ApJS*, **194**, 17
 Reynolds, S. P., Gaensler, B. M., & Bocchino, F. 2012, *SSRv*, **166**, 231
 Rishbeth, H. 1958, *AuJPh*, **11**, 550
 Scott, J. S., & Chevalier, R. A. 1975, *ApJL*, **197**, L5
 Slane, P. O., Castro, D., Funk, S., et al. 2010, *ApJ*, **720**, 266
 Slane, P. O., Hughes, J. P., Temim, T., et al. 2012, *ApJ*, **749**, 131
 Spitkovsky, A. 2008, *ApJL*, **682**, L5
 Strong, A. W., Moskalenko, I. V., & Reimer, O. 2004, *ApJ*, **613**, 962
 Tanaka, T., Allafort, A., Ballet, J., et al. 2011, *ApJL*, **740**, L51
 Thompson, D. J., Fichtel, C. E., Kniffen, D. A., & Ögelman, H. B. 1975, *ApJ*, **200**, L79
 Van Etten, A., & Romani, R. W. 2011, *ApJ*, **742**, 62
 Wallace, P. T., Peterson, B. A., Murdin, P. G., et al. 1977, *Natur*, **266**, 692
 Weiler, K. W., & Pangia, N. 1980, *A&A*, **90**, 269
 Zhang, L., Chen, S. B., & Fang, J. 2008, *ApJ*, **676**, 1210